Control design methods for floating wind turbines for optimal disturbance rejection

Frank Lemmer (né Sandner), David Schlipf and Po Wen Cheng

University of Stuttgart (SWE), Allmandring 5B, 70569 Stuttgart

E-mail: `lemmer@ifb.uni-stuttgart.de`

Abstract. An analysis of the floating wind turbine as a multi-input-multi-output system investigating the effect of the control inputs on the system outputs is shown. These effects are compared to the ones of the disturbances from wind and waves in order to give insights for the selection of the control layout. The frequencies with the largest impact on the outputs due to the limited effect of the controlled variables are identified. Finally, an optimal controller is designed as a benchmark and compared to a conventional PI-controller using only the rotor speed as input. Here, the previously found system properties, especially the difficulties to damp responses to wave excitation, are confirmed and verified through a spectral analysis with realistic environmental conditions. This comparison also assesses the quality of the employed simplified linear simulation model compared to the nonlinear model and shows that such an efficient frequency-domain evaluation for control design is feasible.

1. Introduction

An increasing number of prototypes of floating offshore wind turbines (FOWT) is being developed in Europe, the US and Asia. With these prototypes the design methods and standards improve, which reduces the uncertainty in the design process and supports the progress on the learning curve of this novel technology. This is a main objective of the ongoing research project LIFES50+, in which four commercial platform concepts are upscaled to hold a 10 MW wind turbine. Advanced numerical and experimental methods support this process, which is followed by a detailed design of two selected concepts. Due to the large coupled dynamic response of FOWTs, multi-physics models are necessary. Simplified models are mainly used for system understanding and also for integrated design optimization. The dynamics of conventional oil & gas platforms are usually modeled through a rigid-body model including frequency-domain hydrodynamics. Besides extreme sea-states, the slow-drift motion in medium sea-states is a challenge here for the hull shape and the mooring system design. With the offshore wind turbine mounted on the platform a large and complex rotor-dynamic system is added, which includes dynamics from elastic deformations of the tower and the rotor blades. Also here, the rejection of stochastic loads from wind and waves is key to reducing fatigue loads and stabilizing the power production. The blade-pitch controller for above-rated wind speeds is critical for the overall system stability as it can introduce a negative damping of the tower-top displacement for onshore turbines, as investigated by [1], or, a negative damping of the floating foundation as investigated by, e.g. [2], [3], [4] and both of [5] and [6], who studied different control approaches. Therefore it is necessary to look at the coupled FOWT system including blade-pitch control.

The goal of this paper is to improve blade pitch controllers for better disturbance rejection in wind and waves through a better control layout with more control inputs than the rotor speed. The frequency response to wind and waves is a focus in order to gain system understanding. In offshore engineering the response amplitude operator (RAO) is analyzed, which is the linear disturbance transfer function from the wave height to the six rigid-body degrees of freedom (DOF). With the FOWT such a transfer function from waves but also from wind gives useful insight into the effect of the stochastic wind and wave forces on the platform rigid-body modes but also on the wind turbine drivetrain and therefore the power production. Using methods from control engineering improves the understanding of the system: How does a wind turbine excited by wind and waves of specific frequencies react and which modes of motion yield high loads and should be attenuated by the controller? The wind disturbance rejection problem for floating wind turbines has been studied by [7] with feedforward control using LiDAR measurements. The wave disturbance rejection problem with feedback control was recently studied by [8] and [9] showing that it is difficult to effectively cancel out the wave forces. A multi-input multi-output (MIMO) system analysis can help here to rate the importance of the control inputs generator torque and blade pitch angle with the different (measurable or observable) system outputs for the rejection of wind and wave loads, see [10].

A generic floating platform, originally developed in the project INNWIND.EU, is used with a 10 MW wind turbine, [11], in this work. It will be shortly introduced in section 2. For the numerical analysis a simplified nonlinear FOWT model, developed at the University of Stuttgart is used. It is introduced in section 3. The linearized equations will be applied in section 4: First for a modal analysis and then for an input-output analysis of the system equations. Subsequently, an optimal controller will be designed in section 5 and compared to a conventional single-input-single-output (SISO) controller, comparable to [12] and [13]. Finally, the response spectra from given wind and wave spectra of the design basis of LIFES50+ will be shown, for the linearized system and also from a nonlinear time-domain simulation in section 5.2.
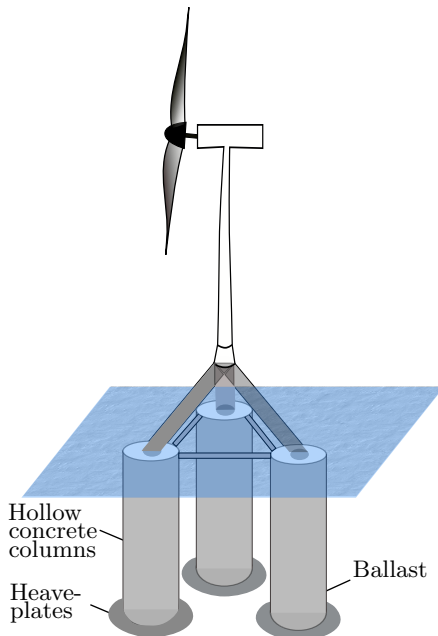

Figure 1: INNWIND.EU TripleSpar concept for DTU 10 MW wind turbine.

Platform draft [m]	54.5
Platform column diameter [m]	15.0
Platform column spacing (to centerline) [m]	26.0
Platform mass [10^6 kg]	28.3
Platform mass moment of inertia about hor. axis @SWL [10^9 kgm^2]	18.7
Platform added mass moment of inertia about hor. axis @SWL [10^9 kgm^2]	10.9
Platform linear damping about hor. axis @SWL [10^9 Nms]	1.5
Number of mooring lines [-]	3
Water depth [m]	180.0
Mooring line length [m]	610.0
Turbine mass [10^6 kg]	1.1
Rated rotor speed [rpm]	9.6
Rated wind speed [m/s]	11.4

Table 1: INNWIND.EU TripleSpar platform and DTU 10 MW wind turbine main parameters.

2. Floating wind turbine concept

The concept used for the analyses of this paper is a generic concrete design from the project INNWIND.EU, see [14]. It consists of three concrete cylinders, comparable to the cylinders of spar-type floating platforms, connected through a steel tripile above the water surface. Figure 1 shows the design with steel heave plates at the lower end of the concrete columns and the steel interface between the upper end of the columns and the tower. The main parameters can be found in table 1. Due to concrete as main material the mass and inertia is significantly higher than for steel platforms. The floating platform rigid-body eigenfrequencies are comparable to other concepts, though, see section 4. The system description is public see [15], as well as the input files[1] for FAST v8 [16]. The concept was published in order to be further developed, improved and detailed by the community.

3. Simulation models

The numerical FOWT model and the sub-models for aerodynamic, hydrodynamic and mooring line forces used for this work are simplified research models focusing on the most significant DOFs, only. They have been developed with the focus of a computationally efficient representation of the overall dynamics for control design and an overview of critical load situations. The models were developed by first simplifying state-of-the-art models keeping the basic nonlinearities. These resulting models show a good agreement with models like FAST, [16]. As a next step the nonlinear models are linearized about the operating point with a reduced validity for the range of system states and inputs for a study on the linear system dynamics.

3.1. Structural models

The employed model is based on a flexible multibody formulation with rigid and flexible bodies. The equations of motion are set up symbolically, depending on the definition of symbolic position vectors as a function of generalized coordinates, and exported to C for a fast model execution. In this work the equations of motion have been set up for five DOFs in 2D: Four rigid DOFs as platform surge x_p, platform heave z_p, platform pitch β_p and rotor azimuth φ combined in $\boldsymbol{q}_r$ and the elastic tower fore-aft deformation x_t in $\boldsymbol{q}_e$

$$\boldsymbol{q} = \begin{bmatrix} x_p \\ z_p \\ \beta_p \\ \varphi \\ x_t \end{bmatrix}, \qquad \boldsymbol{q}_r = \begin{bmatrix} x_p \\ z_p \\ \beta_p \\ \varphi \end{bmatrix}, \qquad \boldsymbol{q}_e = \begin{bmatrix} x_t \end{bmatrix}. \qquad (1)$$

For a state-space description the state vector $\boldsymbol{x}$ results with the rotor speed Ω as

$$\boldsymbol{x} = \begin{bmatrix} x_p, z_p, \beta_p, \varphi, x_t, \dot{x}_p, \dot{z}_p, \dot{\beta}_p, \Omega, \dot{x}_t \end{bmatrix}^T. \qquad (2)$$

These DOFs are selected in order to reduce the system to the most important dynamics, which are critical for conceptual design and control. Therefore, side-side dynamics (and every motion in lateral direction) are neglected following the recommendation of [17]. Also disturbances will only act in axial direction (x), see figure 2. The rigid bodies are the *platform*, *nacelle* and the *rotor* and the only elastic body is the *tower*. The tower shape function used is the first fore-aft mode shape. The individual rotor blades are not included in this model but the rotor is modeled as a rigid disk. This method neglects the coupling of flapwise blade dynamics with the tower modes. It is still used here because it simplifies the model to a significant extent and allows a clearer view on the main system dynamics.

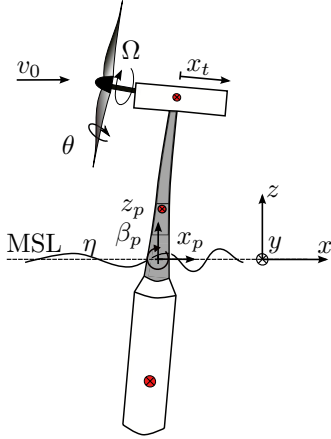[1] http://www.ifb.uni-stuttgart.de/windenergie/downloads

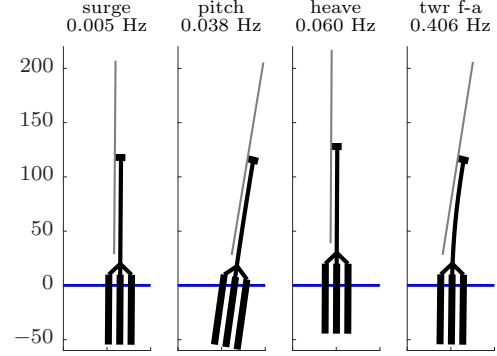Figure 2: General topology of the simplified multibody system.

Figure 3: Mode shapes of simplified model.

The three catenary mooring lines are represented by a nonlinear quasi-static model, which is based on the mooring line formulation of FAST v7, see [18]. It gives, for each mooring line, the horizontal and vertical forces on the platform depending on its position. For the linearization a perturbation analysis is done at the respective operating point resulting in a 6×6 stiffness matrix. The still-water hydrodynamics are represented through a constant added-mass in all considered directions, interpolated at the eigenfrequency of the respective DOF of the frequency-dependent panel-code results. Radiation memory effects are neglected as they are usually small for FOWTs.

The symbolic equations of motion are linearized analytically about the set point of the states $\boldsymbol{x}_0$ and the inputs $\boldsymbol{u}_0$

$$\boldsymbol{x} = \boldsymbol{x}_0 + \Delta \boldsymbol{x} \qquad\qquad \boldsymbol{u} = \boldsymbol{u}_0 + \Delta \boldsymbol{u}, \tag{3}$$

where $\Delta \boldsymbol{x}$ and $\Delta \boldsymbol{u}$ are the new vectors of differential states and inputs, respectively. For simplicity, the Δ is omitted in the following, where we always talk about the differential states, inputs and outputs. The coupled nonlinear equations of motion in state-space description can be separated for position- and velocity-dependent terms. It remains with the input matrix $\boldsymbol{B}$ and the identity matrix $\boldsymbol{E}$

$$\dot{\boldsymbol{x}} = \underbrace{\begin{bmatrix} \boldsymbol{0} & \boldsymbol{E} \\ -\boldsymbol{M}^{-1}\boldsymbol{Q} & -\boldsymbol{M}^{-1}\boldsymbol{P} \end{bmatrix}}_{\boldsymbol{A}} \boldsymbol{x} + \boldsymbol{B}\boldsymbol{u}. \tag{4}$$

One can identify the position-dependent matrix $\boldsymbol{Q}$ and the velocity-dependent matrix $\boldsymbol{P}$, which result from the transformation of the vector of Coriolis, centrifugal and gyroscopic forces and the applied forces. The linearization is especially critical for the aerodynamic force coefficients due to the high nonlinearity. A more detailed introduction to the model is given in [19] and [20].

3.2. Disturbance models

External disturbances on the model arise from wind and waves. The aerodynamic thrust force and torque are calculated based on thrust and power coefficients depending on the tip-speed ratio λ and the blade-pitch angle θ. These coefficients have to be calculated using blade-element

momentum theory (BEM) as a pre-processing step. During runtime the relative rotor-effective wind speed v_0 is used to calculate the aerodynamic forces. The aerodynamic coefficients are highly nonlinear depending on the angle of attack, which in turn, depends on the tip-speed ratio and the blade pitch angle. Therefore, the linearization is only valid close to the operating point. The derivation of the linear aerodynamic coefficients can be found in [13]. The aerodynamic model uses the rotor-effective wind speed v_0 as input, which is the scalar wind speed relative to the rotor-plane, calculated by filtering the three-dimensional turbulent wind field to get only the components which excite the drivetrain rotation, see [21]. This means that the rotational DOF of the rotor is prioritized over the tower-top displacement x_t. The filtering of the turbulent wind speed can yield less high-frequency excitation of the tower and underestimate the tower fatigue loads, see [22]. In summary, the model neglects dynamic inflow and dynamic stall effects, any dependency on the rotor azimuth angle and effects from blade deformation. These simplifications allow for a clear representation of the main aerodynamic sensitivities, which means derivatives with respect to the wind speed $\frac{\partial(*)}{\partial v}$, and to the blade pitch angle $\frac{\partial(*)}{\partial \theta}$ and rotor speed $\frac{\partial(*)}{\partial \Omega}$.

The frequency-dependent wave excitation force vectors are calculated by a hydrodynamic panel code. The resulting frequency-domain representation of the six forces on the (fixed) floating body is subject to a system identification problem giving a parametric linear transfer function. The approach is detailed in [20]. Eventually, both disturbance models can be included in the nonlinear time-domain model as well as the linearized system description. Both use only the scalar inputs of rotor-effective wind speed v_0 and incident wave height η_0, see figure 4. The linear system without control will be analyzed in the next section.

4. Linear system analysis without feedback control

In this section the system properties will be first presented through an eigenanalysis. An input-output (I/O) scaling will then allow for a better quantization of the effects of different system inputs on the outputs. The disturbance transfer functions will give an insight into the effects of wind and waves compared to the available control inputs. The FOWT model is here seen as a MIMO system, meaning that various system inputs $\boldsymbol{u}$ determine the system outputs $\boldsymbol{y}$. The vector $\boldsymbol{u}$ consist of control and disturbance inputs $\boldsymbol{u} = [\boldsymbol{u}_c, \boldsymbol{u}_d]^T$. As outputs different system states of the state vector $\boldsymbol{x}$ will be considered. Figure 4 shows the basic open-loop (OL) configuration of the linear system. In our case the coupled system transfer function $\boldsymbol{G}(s)$ is not diagonal but coupled, which means that also off-diagonal elements are present and using one control input, like the generator torque M_g does not only affect the rotor speed Ω but also other states like the tower-top displacement x_t or the platform pitch angle β_p.

The mode shapes are visualized in figure 3 together with the respective eigenfrequencies at a mean wind speed $\bar{v} = 13.9\,\mathrm{m/s}$. These main system frequencies will be highlighted in all of the following graphs. The poles and zeros of the SISO transfer function from blade pitch angle θ to the rotor speed Ω are shown in the pole-zero map in figure 5. The zeros in the right-half-plane (RHPZ), with $\mathrm{Re} > 0$, close to the tower eigenfrequency can be seen. For wind speeds closer to rated there are also two complex conjugate RHPZ at the platform pitch eigenfrequency, in figure 5 they are right next to the imaginary axis in the left half plane. The RHPZ yield an inverse response behavior, which poses a hard constraint for control design, especially if only SISO control is used. Then it can be remedied by limiting the control bandwidth to frequencies below this RHPZ, which, on the other hand, reduces the controller performance. This RHPZ for wind turbines in general has been investigated by [1] and by [3] for floating wind turbines. The platform pitch poles are especially critical for the system dynamics, as well as the tower fore-aft poles, since they are highly coupled with the drivetrain. The surge mode is usually highly damped and at a very low frequency for platforms with catenary mooring lines, which can be a problem with second order slow-drift wave excitation. The platform heave mode does not pose problems since it is almost completely decoupled from the drivetrain.
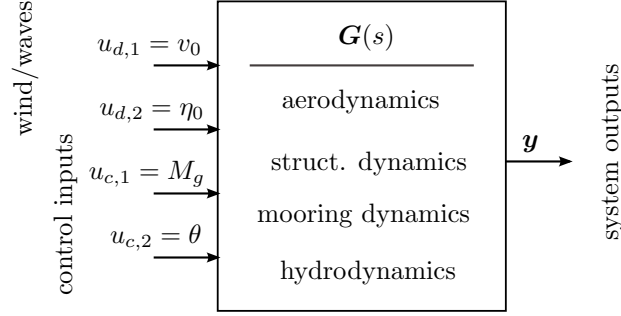
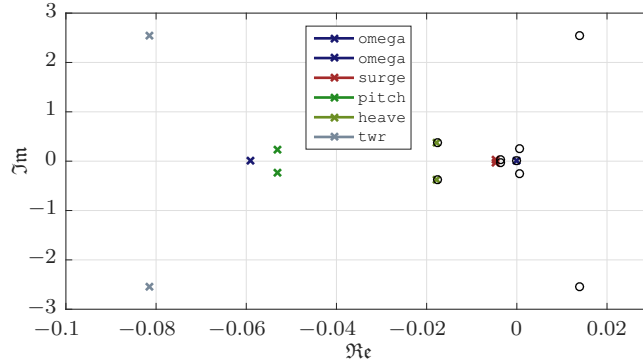Figure 4: FOWT system block diagram with SISO control.

Figure 5: Pole-zero map of SISO transfer function from blade pitch angle θ to rotor speed Ω (poles ×, zeros ○).

Next, an input-output scaling will be applied to the transfer function from disturbance inputs $\boldsymbol{u}_d$ and control inputs $\boldsymbol{u}_c$ to the outputs $\boldsymbol{y}$. This allows for a quantization and comparison of the effects from the different system inputs $\boldsymbol{u}$ as shown in the next section. The scaling law remains for the dimensionless system transfer function $\hat{\boldsymbol{G}}$ following [10] as

$$\hat{\boldsymbol{G}} = \boldsymbol{D}_y^{-1}\boldsymbol{G}\boldsymbol{D}_u. \tag{5}$$

The scaling matrices for inputs $\boldsymbol{D}_u$ and for outputs $\boldsymbol{D}_y$ have been selected based on maximum allowed or desired excursions, mostly based on the operating point of inputs $\boldsymbol{u}_0$ and states $\boldsymbol{x}_0$ as

$$\boldsymbol{D}_u = \begin{bmatrix} 0.1\,M_{g,0} & 0 & 0 & 0 \\ 0 & 5.0\frac{\pi}{180} & 0 & 0 \\ 0 & 0 & 0.1\,\bar{v} & 0 \\ 0 & 0 & 0 & 4.0 \end{bmatrix} \qquad \boldsymbol{D}_y = \begin{bmatrix} 0.13\,\Omega_0 & 0 \\ 0 & 0.5\,x_{t,0} \end{bmatrix} \tag{6}$$

4.1. Control and disturbance inputs to outputs

Figure 6 shows the scaled transfer function bode diagram for the control inputs $\boldsymbol{u}_c = [M_g, \theta]^T$ and the outputs $\boldsymbol{y} = [\Omega, x_t]^T$ at a wind speed of $\bar{v} = 13.9\,\mathrm{m/s}$. This MIMO transfer function matrix gives good insight into the diagonal and cross-coupling dynamics of the system. With this MIMO description the zeros (and RHPZ) seen for the SISO transfer function from blade pitch angle θ to rotor speed Ω of figure 5 are no longer visible. However, the transfer function matrix $\boldsymbol{G}$ can loose rank at frequencies of MIMO zeros. On the top right graph the frequency-dependent effect of, e.g., the blade pitch angle (which is the main control input for above rated

wind speeds) on the rotor speed Ω can be seen. A smaller amplification of the sinusoidal blade pitch angle on the rotor speed is visible when getting close to the tower eigenfrequency. This is due to the rotor inertia, which attenuates any high-frequency excitation. Staying in the right column but now looking at the lower graph shows that changing the blade pitch angle does not only result in a change of the rotor speed but also of the tower-top displacement x_t, which is the reason why a decoupling, diagonal controller is hardly feasible for wind turbines. The generator torque (left column) shows about five times less amplification on the rotor speed than the blade pitch angle and even more, about twenty times less amplification on the tower-top displacement. This is generally advantageous as one could decouple the system and control the rotor speed with the generator and the tower-top displacement with the blade pitch angle. The same can be found analyzing the relative gain array (RGA), see [10]. Unfortunately, the actuator constraints prohibit such a realization, since the generator is usually not designed with an excessive safety factor on the electrical current and therefore only small fluctuations of the torque at rated wind speed are allowed.

In a next step the same transfer function matrix is shown but now with the disturbance inputs $\boldsymbol{u}_d$ in order to see how much the outputs $\boldsymbol{y}$ are affected by wind and waves and to which extent the control inputs $\boldsymbol{u}_c$ can reduce these effects. Figure 7 shows the scaled disturbance transfer function Bode diagram with the disturbance inputs $\boldsymbol{u}_d = [v_0, \eta_0]^T$ and the outputs $\boldsymbol{y} = [\Omega, x_t]^T$ at the wind speed $\bar{v} = 13.9\,\mathrm{m/s}$. Generally, both scaled disturbances have a comparable effect on the scaled outputs. The cut-off frequency of the rotor speed on the top-left is in the same range as for the blade pitch angle. The waves mostly affect the rotor speed at the platform surge and around the platform pitch eigenfrequency. The tower-top displacement is excited by the wind (lower-left) mostly at its eigenfrequency but also at the other platform frequencies for the waves (lower-right). Although there is a trough visible at the lower-right plot at the peak wave frequency used here ($f_{wave} \approx 0.1\,\mathrm{Hz}$) this excitation of the tower from waves is not negligible.

This open-loop analysis can be also done systematically through a singular-value decomposition (SVD), see [10]. The SVD shows the strongest and weakest input directions $\boldsymbol{V}$ and output directions $\boldsymbol{U}$ together with the associated amplifications $\boldsymbol{\sigma}$. With the system $\hat{\boldsymbol{G}}$ considered here with the control inputs $\boldsymbol{u}_c = [M_g, \theta]^T$ and outputs $\boldsymbol{y} = [\Omega, x_t]^T$ one can investigate the combination of the inputs that yield the highest gain on the outputs. This gain $\boldsymbol{\sigma}$ is associated with the strongest output direction. On top of figure 8 one can see that the strongest singular value (SV) in dark color contains only a little contribution of the generator torque M_g but a high portion of the blade pitch angle θ, which confirms the findings from the I/O transfer function matrix of figure 6. Looking at frequencies up to the platform pitch eigenfrequency this input direction affects mostly the rotor speed Ω with a decreasing gain. Above the platform pitch eigenfrequency the strongest output direction (second row, dark color) points again towards the rotor speed Ω with a peak at a MIMO-zero, before the strongest input affects more the tower at higher frequencies up to the tower eigenfrequency.

One can assess the effect of using the two control inputs (M_g, θ) as compared to blade pitch angle only: The strongest SV yields slightly higher gains (figure 8, bottom) than the blade pitch angle only (figure 6, upper right). Consequently, the generator torque is a useful actuator, although figure 6 (left column) shows very small gains associated with M_g. The strongest (control) output direction (figure 8) can now be compared to the output disturbance directions from wind and waves (figure 9). For low frequencies wind and waves affect more the rotor speed than the tower-top displacement (figure 9, top). Interesting are now the gains of the disturbance output directions, compared to the strongest control output directions: One can see that the gain of the strongest control input (figure 8, bottom) is of about half the magnitude as the gain from wind on the outputs (figure 9, middle left). For the waves it is different: The amplifications of the waves on the outputs is of comparable magnitude as of the control inputs. This is confirmed
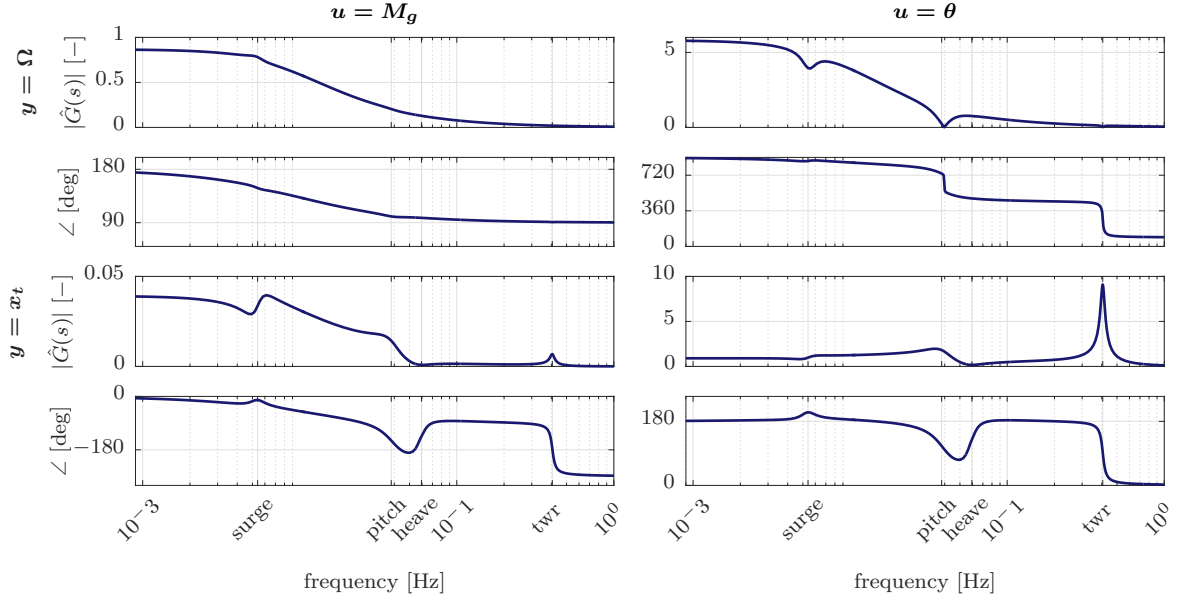
Figure 6: I/O transfer function Bode diagram with inputs $\boldsymbol{u}_c = [M_g, \theta]^T$ and outputs $\boldsymbol{y} = [\Omega, x_t]^T$ @$v_0 = 13.9\,\text{m/s}$, scaled.
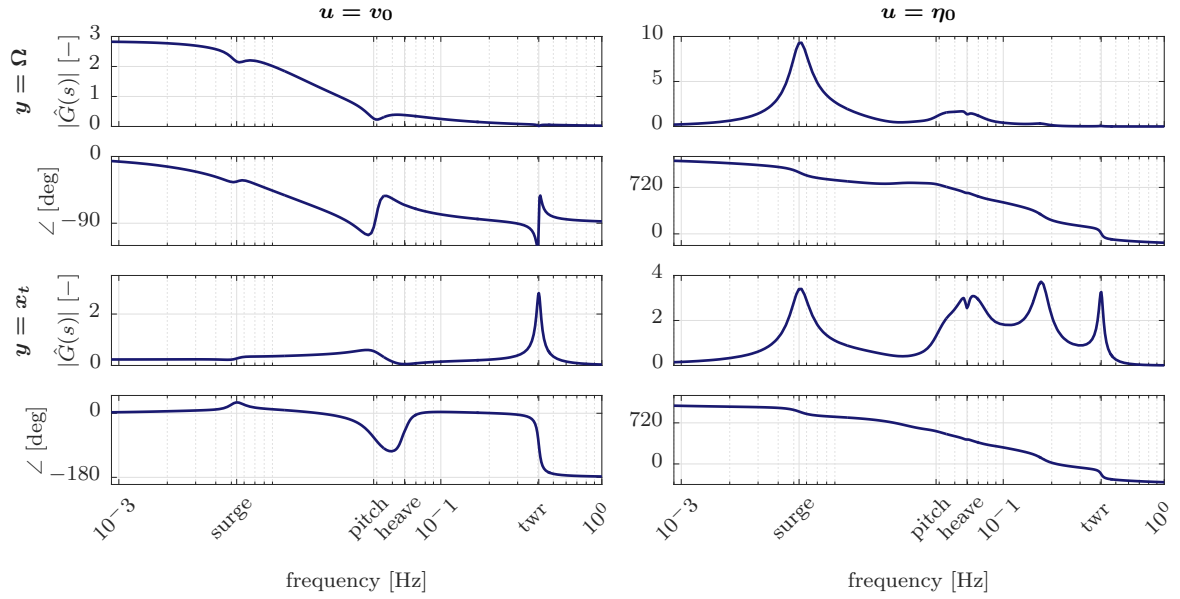

Figure 7: Open-loop disturbance transfer function Bode diagram with inputs $\boldsymbol{u} = [v_0, \eta_0]^T$ and outputs $\boldsymbol{y} = [\Omega, x_t]^T$ @$v_0 = 13.9\,\text{m/s}$, scaled.

by the disturbance condition number γ, which takes high values if the disturbance direction is aligned with the weakest control output direction. This means that it is high if the disturbance affects directions which are hard to control, see [10]. Here, this is the case for wind excitations of high frequencies and for waves, around the MIMO zero at $0.05\,\text{Hz}$, see figure 9, bottom row. This analysis shows that waves significantly impact the rotor speed Ω and the tower-top displacement x_t and it is difficult to counteract these excitations with θ and M_g.
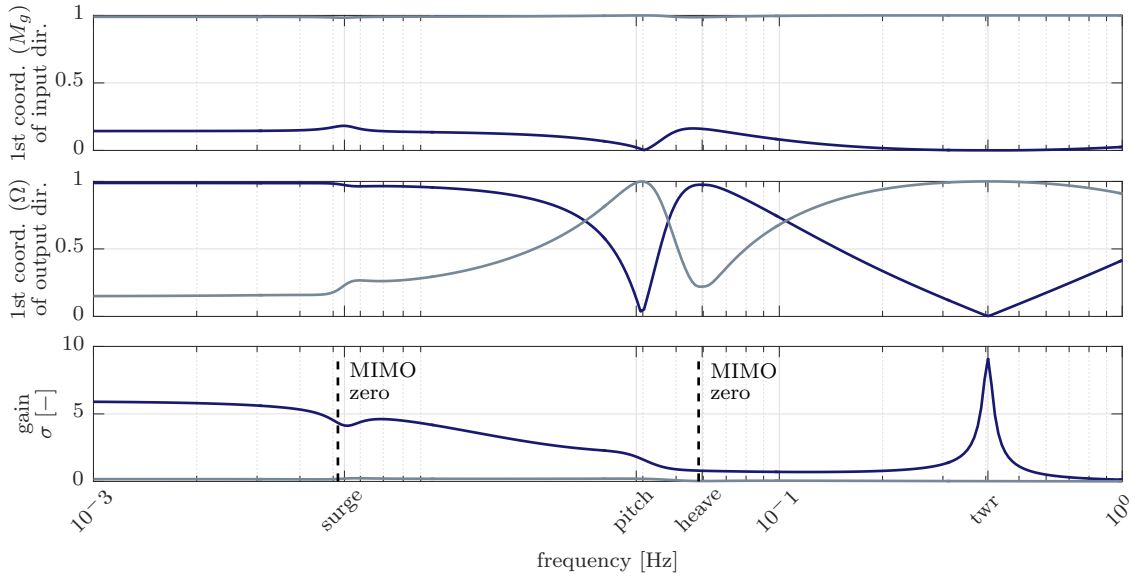
Figure 8: Singular-value decomposition of I/O transfer function: Strongest (dark) and weakest (lite) input and output directions with associated gains: The first plot shows the first coordinate of the input coordinates $\boldsymbol{u} = [M_g, \theta]^T$ and the second plot the first coordinate of the output coordinates $\boldsymbol{y} = [\Omega, x_t]^T$ @$v_0 = 13.9\,\mathrm{m/s}$, the third plot shows the gain associated with the strongest and weakest direction and the MIMO zeros of $\boldsymbol{G}$.
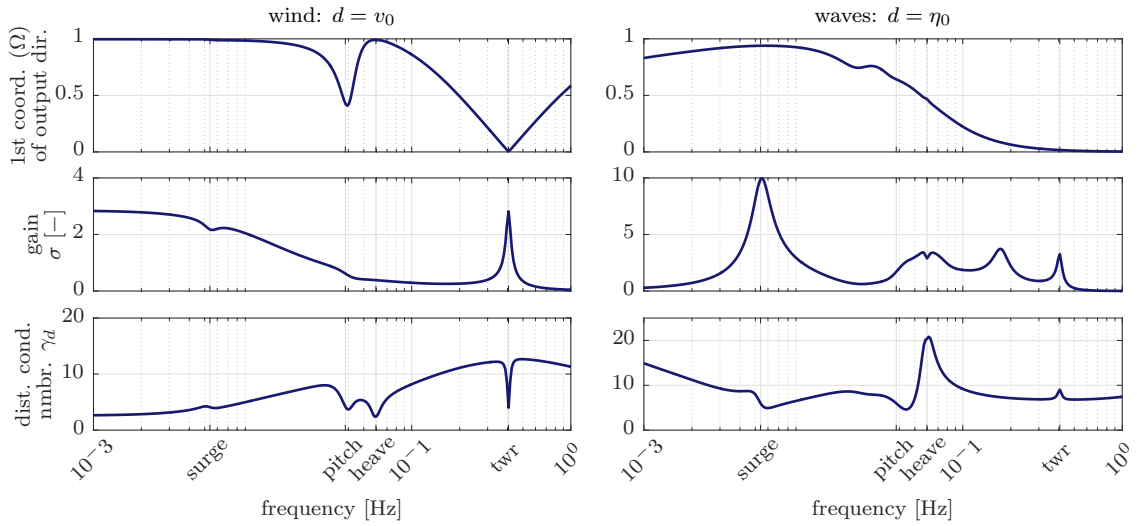

Figure 9: Singular-value decomposition of open-loop disturbance transfer function for wind (left) and waves (right): The first row shows the first coordinate of the output coordinates $\boldsymbol{y} = [\Omega, x_t]^T$, the second row shows the associated gain and the third plot shows the disturbance condition number γ_d.

5. Linear system analysis with feedback control

A conventional SISO controller, designed in [22], will be presented and an optimal model-based Linear Quadratic Regulator (LQR) will be designed assuming full state knowledge as a benchmark for comparison.

Table 2: Comparisons of feedback gains of LQR and SISO controller @ $\bar{v} = 13.9\,\mathrm{m/s}$.

	K_{x_p}	K_{z_p}	K_{β_p}	K_φ	K_{x_t}	$K_{\dot{x}_p}$	$K_{\dot{z}_p}$	$K_{\dot{\beta}_p}$	K_Ω	$K_{\dot{x}_t}$
$-\boldsymbol{K}_{lqr,\theta}$	0.0	0.0	0.7	0.043	-0.02	0.02	0.0	-0.9	0.52	0.057
$\boldsymbol{K}_{SISO,PI}$	0.0	0.0	0.0	0.054	0.0	0.0	0.0	0.0	0.54	0.0

5.1. Control design

For SISO control (rotor speed error to blade pitch angle) of FOWTs usually the bandwidth is reduced in order to mitigate the effects from the RHPZ, see [2] and [4]. The SISO controller used here is designed by determining the PI control gains such that the coupled platform pitch pole has a given real-part close to the stability limit. This results in an optimal compromise of rotor speed tracking and platform stability, see [15].

As a benchmark of a MIMO controller an LQR is designed using the blade pitch angle and the generator torque as control inputs. Such optimal controllers have been already applied to floating wind turbines as in [13], [23] and [24]. The LQR minimizes a quadratic cost function J of a linear model with weights on the control inputs $\boldsymbol{u}_c$ and outputs $\boldsymbol{y}$, see [10] as

$$J = \lim_{T \to \infty} \frac{1}{T} \int_0^T \left[\boldsymbol{x}^T \boldsymbol{Q} \boldsymbol{x} + \boldsymbol{u}_c^T \boldsymbol{R} \boldsymbol{u}_c \right] dt. \tag{7}$$

The weights $\boldsymbol{R}$ on the inputs $\boldsymbol{u}_c$, and the weights $\boldsymbol{Q}$ on the states $\boldsymbol{x}$ are selected through brute-force optimizations at various environmental conditions above rated as

$$\boldsymbol{R} = \mathrm{diag}\left(\begin{bmatrix} \dfrac{0.05}{M_{g,0}^2}, & \dfrac{0.04}{\left(5.0\frac{\pi}{180}\right)^2} \end{bmatrix} \right) \tag{8}$$

$$\boldsymbol{Q} = \mathrm{diag}\left(\begin{bmatrix} 0.0, & 0.0, & 0.0, & \dfrac{1.0}{(10.0\,\Omega_0)^2}, & 0.0, & 0.0, & 0.0, & 0.0, & \dfrac{1.0}{\Omega_0^2}, & \dfrac{0.05}{(0.5\,\omega_{eig,twr})^2} \end{bmatrix} \right). \tag{9}$$

This results in the state feedback matrix $\boldsymbol{K}_{lqr}$ by solving the Riccati equation

$$\boldsymbol{u}_c(t) = -\boldsymbol{K}_{lqr} \boldsymbol{x}(t). \tag{10}$$

Integral action has been included on the rotor speed signal since the rotor azimuth $\varphi = x(5)$ is part of the state vector $\boldsymbol{x}$. Usually, the state signals as inputs to the LQR need to be calculated by an observer. In this work, however, the states are assumed to be perfectly measurable in order to see the optimal control performance as a benchmark for comparison. The optimal state feedback matrix $\boldsymbol{K}_{lqr}$ has been calculated for the same cost function with only the blade pitch angle as input, in order to compare the gains to the SISO controller, see table 2. Interestingly, the feedback of the tower-top velocity $\dot{x}_t$ is positive as expected (the blade pitch angle increases when the nacelle velocity is positive) but the feedback of the platform pitch velocity $\dot{\beta}_p$ is negative and only the one of its integral, β_p is positive. The gains of the rotor speed Ω and the azimuth angle φ are well comparable to the SISO-PI controller.

5.2. System analysis

The closed-loop systems including the different controllers will be compared in this section. Figure 10 shows the complementary sensitivity $T(j\omega)$ or the transfer function from the reference rotor speed Ω_{ref} to the output rotor speed Ω. Here, the bandwidth of the controllers can be
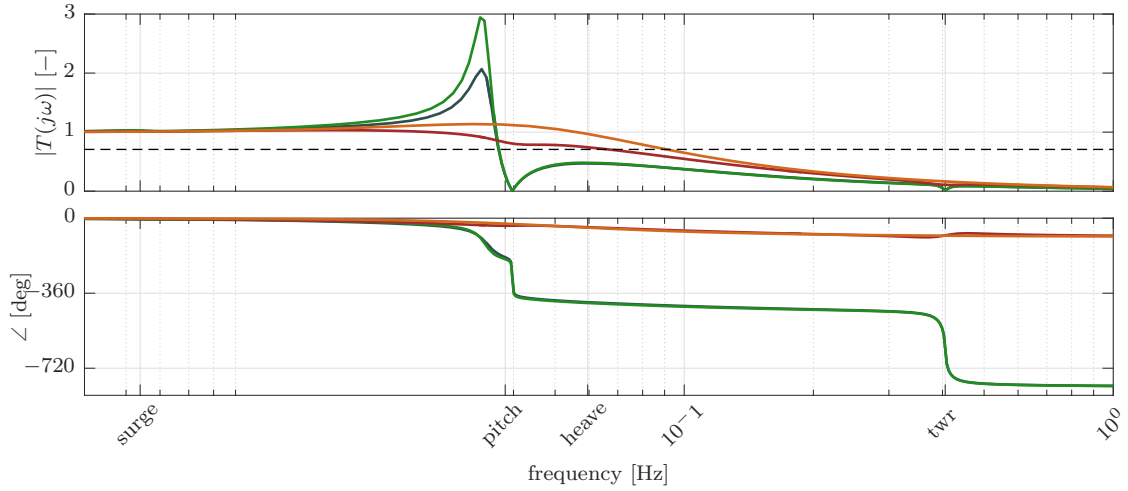
Figure 10: Complementary sensitivity functions (transfer function from Ω_{ref} to Ω) for LQR (dark red), PI-SISO through integrated design, [12] (dark grey), PI-SISO control with detuned gains (green), and equivalent onshore controller for drivetrain only (orange).

compared. Additionally to the SISO controller and the LQR, a PI-controller has been included using a model of the drivetrain only (no floating platform, tower) with a drivetrain-closed-loop eigenfrequency of $\omega_{drive,CL} = 0.3\,\text{rad/s}$ and a damping ratio of $\xi_{drive,CL} = 0.7\,[-]$ (orange). Also, a PI-SISO controller with "detuned gains", according to [4] with a drivetrain-closed-loop eigenfrequency $\omega_{drive,CL}$ proportional to the platform pitch eigenfrequency ω_{eig,β_p} of $\omega_{drive,CL} = 0.8\,\omega_{eig,\beta_p}$ has been designed (green). For the SISO controllers the zero at the platform pitch eigenfrequency is well visible, which determines also the bandwidth (crossing at $|T(j\omega)| = 0.707$). The LQR (dark red) on the other hand shows an increased bandwidth and no phase loss at the platform pitch and the tower eigenfrequencies, showing the effect of the MIMO feedback. The bandwidth is only slightly decreased compared to the drivetrain-only system.

5.3. Response to wind and waves

The sensitivity function $\boldsymbol{S}(j\omega)$ is the transfer function from the disturbance inputs $\boldsymbol{d}$ to the system outputs $\boldsymbol{y}$. It is now analyzed with the closed-loop system and shows how wind and waves affect the FOWT. Figure 11 shows the transfer functions from wind speed v_0 in the left column and from the wave height η_0 in the right column. The results for the LQR (red) are significantly better, especially at the platform pitch and tower eigenfrequencies. However, at the wave frequency $f_{wave} = 0.1\,\text{Hz}$ there is no visible improvement with the LQR. This is aligned with the issues encountered by [8] and confirms also the findings of the open-loop analyses of section 4, where a high disturbance condition number γ was found slightly below the wave frequency. The open-loop disturbance transfer function, figure 7 also showed large effects of the waves on the rotor speed proving that it is difficult to damp the excitations from the waves.

As a last step the load power spectral density S_y of the system outputs will be calculated using the linear frequency-domain model with realistic wind and wave spectra as inputs. This method allows a very efficient evaluation of new controllers as no computationally expensive time-domain simulations are necessary but only a multiplication of disturbance spectra S_d with the squared transfer functions G_d^2

$$S_\Omega = G_{v_0 \to \Omega}^2 S_{d,v_0} + G_{\eta_0 \to \Omega}^2 S_{d,\eta_0} \tag{11}$$

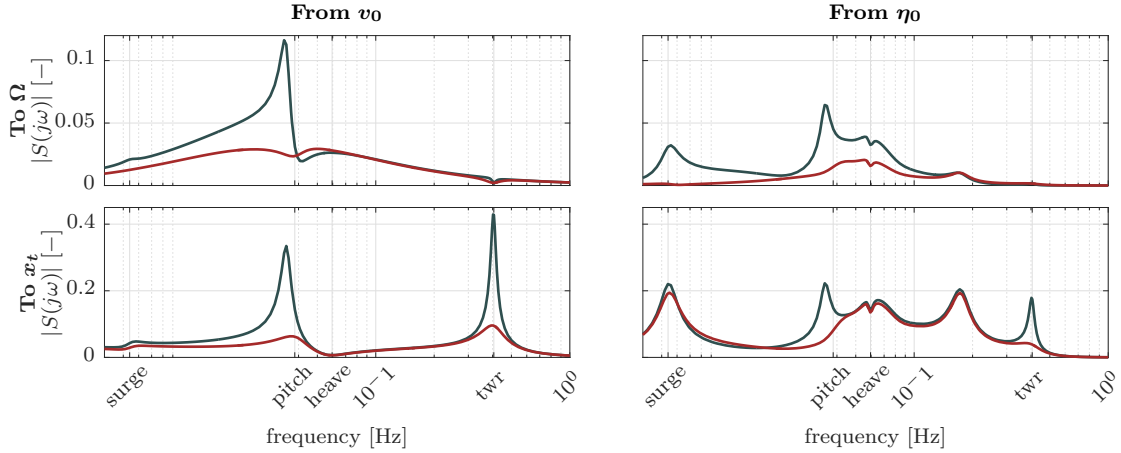Figure 11: Sensitivity functions (transfer functions from $\boldsymbol{u} = [v_0, \eta_0]$ to $\boldsymbol{y} = [\Omega, x_t]$ for LQR (dark red) and PI-SISO control, [12] (grey).

and

$$S_{x_t} = G^2_{v_0 \to x_t} S_{d,v_0} + G^2_{\eta_0 \to x_t} S_{d,\eta_0}. \tag{12}$$

Due to the linearization this involves naturally errors depending on the deviation of inputs and states from the operating point. Figure 12 shows the wind and wave frequency-domain spectra S_d for a realistic load case of the design basis of LIFES50+, [25] at $\bar{v} = 13.9\,\mathrm{m/s}$ in the left column. On the top left an analytical result of the rotor-effective wind speed v_0 from the 3D turbulent wind field according to [21] is shown along with the result from timeseries. In the right column the spectra of the rotor speed Ω and the tower-top displacement x_t are shown, first from the linear model and second, from a Fourier transform of the nonlinear time-domain results. It can be seen that the difference between the LQR and the SISO controller is well captured by the linear model. Only slight deviations are visible between the frequency-domain model and the nonlinear time-domain model, mostly around and above the wave frequency of $f_{wave} = 0.1\,\mathrm{Hz}$. For the SISO controller more differences are visible between the models at low frequencies, which is likely due to the larger deviations from the operating point. In conclusion, it can be seen that this method is promising. Nonlinear and transient effects, at least for this simplified model, appear not to be dominant, which allows to use frequency-domain methods for controller tuning of FOWTs.

6. Conclusions

A thorough system analysis of a floating wind turbine has been performed considering the MIMO description including control inputs and disturbances for the open-loop case. Especially the wave disturbance could be included here through a previously developed parametric model for first-order wave loads, which allows to assess the coupled system frequency response at realistic environmental conditions. It has been shown which "output directions" are critically affected by wind and wave loads due to the limited effect of the actuated variables in these directions. The blade pitch angle can most effectively control rotor speed and tower-top displacement for low frequencies, whereas the generator torque has a much smaller impact. However, the generator torque, together with the blade pitch angle (multi-input), can effectively mitigate the present right-half plane zero. A linear quadratic regulator (LQR) assuming perfect state measurements has been designed. The comparison to a previously developed SISO-controller shows that the LQR can significantly reduce the system responses and attenuate various resonances. However, even the LQR, can hardly attenuate the excitations from the waves,
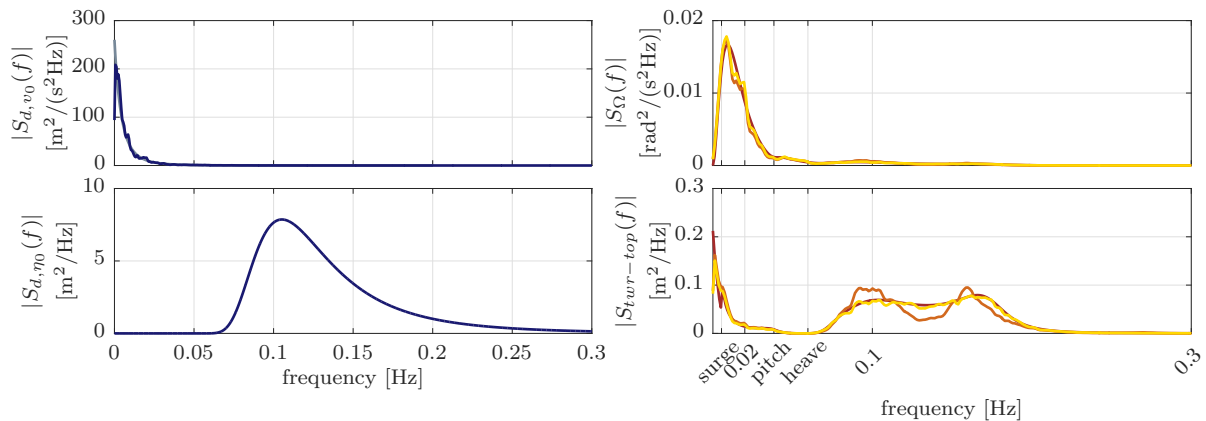
Figure 12: Left column: Disturbance spectra of wind speed v_0 and wave height η_0 (analytic: lite color; timeseries: dark color). Right column: Output spectra of rotor speed Ω (top) and tower-top displacement x_t (bottom) from linear frequency-domain model (dark red), nonlinear time-domain (light red) and linear time-domain simulation (yellow) with LQR controller. Turbulent wind of $\bar{v} = 13.9\,\mathrm{m/s}$ of Kaimal spectrum with turbulence intensity $TI = 13.8\,\%$ and wave spectrum with significant wave height $H_s = 3\,\mathrm{m}$ and peak spectral period $T_p = 9.5\,\mathrm{s}$.

which confirms the results of the preceding MIMO analyses of the open loop. The comparison of nonlinear time-domain simulations with linear frequency-domain calculations showed good agreement, which endorses the use of these computationally efficient methods for controller tuning under realistic environmental conditions. In further steps such lessons on limitations of the control actuators at certain frequencies can be taken into account for a design which mitigates the critical responses, also through the formulation of an optimization problem. This will be subject of further studies in LIFES50+.

Acknowledgements

References

[1] Leithead, W., and Dominguez, S., 2006. "Coordinated Control Design for Wind Turbine Control Systems". In Proceedings of the EWEC.

[2] Larsen, T. J., and Hanson, T. D., 2007. "A method to avoid negative damped low frequent tower vibrations for a floating, pitch controlled wind turbine". *Journal of Physics: Conference Series,* **75**.

[3] Fischer, B., 2012. "Reducing rotor speed variations of floating wind turbines by compensation of non-minimum phase zeros". In Proceedings of the EWEA, pp. 144–147.

[4] Jonkman, J., 2008. "Influence of Control on the Pitch Damping of a Floating Wind Turbine". In Proceedings of the ASME Wind Energy Symposium.

[5] Fleming, P., Pineda, I., Rossetti, M., Wright, A., and Arora, D., 2014. "Evaluating Methods For Control Of An Offshore Floating Turbine". In Proceedings of the ASME 33rd International Conference on Ocean, Offshore and Arctic Engineering.

[6] Savenije, F., and Peeringa, J., 2014. "Control development for floating wind". *Journal of Physics: Conference Series,* **524**.

[7] Schlipf, D., Simley, E., Lemmer, F., Pao, L., and Cheng, P. W., 2015. "Collective Pitch Feedforward Control of Floating Wind Turbines Using Lidar". *Journal of Ocean and Wind Energy,* **2**(4), pp. 223–230.

[8] Fleming, P., Peiffer, A., and Schlipf, D., 2016. "Wind Turbine Controller To Mitigate Structural Loads On A

Floating Wind Turbine Platform". In Proceedings of the ASME 35th International Conference on Ocean, Offshore and Arctic Engineering.

[9] Namik, H., 2012. "Individual Blade Pitch and Disturbance Accommodating Control of Floating Offshore Wind Turbines". PhD thesis, University of Auckland.

[10] Skogestad, S., and Postlethwaite, I., 2007. *Multivariable feedback control: Analysis and design.* John Wiley and Sons, Chichester.

[11] Bak, C., Zahle, F., Bitsche, R., Kim, T., Yde, A., Henriksen, L., Natarajan, A., and Hansen, M., 2013. Description of the DTU 10 MW Reference Wind Turbine. Tech. rep., DTU Wind Energy.

[12] Sandner, F., Schlipf, D., Matha, D., and Cheng, P. W., 2014. "Integrated Optimization Of Floating Wind Turbine Systems". In Proceedings of the ASME 33rd International Conference on Ocean, Offshore and Arctic Engineering.

[13] Lemmer, F., Raach, S., Schlipf, D., and Cheng, P. W., 2015. "Prospects of Linear Model Predictive Control on a 10MW Floating Wind Turbine". In Proceedings of the ASME 34th International Conference on Ocean, Offshore and Arctic Engineering.

[14] Azcona, J., Lemmer, F., Amann, F., Voutsinas, S., and Savenije, F., 2016. INNWIND.EU D4.37: Design Solutions for 10MW Floating Offshore Wind Turbines (to be published). Tech. rep., CENER.

[15] Lemmer, F., Amann, F., Raach, S., and Schlipf, D., 2016. Definition of the SWE-TripleSpar Floating Platform for the DTU 10MW Reference Wind Turbine. Tech. rep., University of Stuttgart.

[16] NWTC, 2016. NWTC Information Portal (FAST v8).

[17] Barj, L., Stewart, S., Stewart, G., Lackner, M., Jonkman, J., Robertson, A., and Matha, D., 2014. "Wind/Wave Misalignment in the Loads Analysis of a Floating Offshore Wind Turbine". In Proceedings of the AIAA.

[18] Jonkman, J., and Buhl, M., 2005. *Fast User's Guide.* NREL.

[19] Sandner, F., Schlipf, D., Matha, D., Seifried, R., and Cheng, P. W., 2012. "Reduced Nonlinear Model of a Spar-Mounted Floating Wind Turbine". In Proceedings of the German Wind Energy Conference DEWEK.

[20] Lemmer, F., Raach, S., Schlipf, D., and Cheng, P. W., 2016. "Parametric Wave Excitation Model for Floating Wind Turbines". *Energy Procedia.*

[21] Schlipf, D., Cheng, P. W., and Mann, J., 2013. "Model of the Correlation between Lidar Systems and Wind Turbines for Lidar-Assisted Control". *Journal of Atmospheric and Oceanic Technology,* **30**(10), oct, pp. 2233–2240.

[22] Lemmer, F., Müller, K., Pegalajar-Jurado, A., Borg, M., and Bredmose, H., 2016. LIFES50+ D4.1: Simple Numerical Models for Upscaled Design. Tech. rep., University of Stuttgart.

[23] de Corcuera, A. D., Pujana-Arrese, A., Ezquerra, J. M., Segurola, E., and Landaluze, J., 2012. "H∞-based control for load mitigation in wind turbines". *Energies,* **5**(4), pp. 938–967.

[24] Lindeberg, E., 2009. "Optimal Control of Floating Offshore Wind Turbines". MSc thesis, Norwegian University of Science and Technology.

[25] Krieger, A., Ramachandran, G. K. V., Vita, L., Gómez Alonso, P., Berque, J., and Aguirre-Suso, G., 2016. Qualification of innovative floating substructures for 10MW wind turbines and water depths greater than 50m. Tech. rep., DNV-GL.